









# The JWST EXCELS survey: tracing the chemical enrichment pathways of high-redshift star-forming galaxies with O, Ar and Ne abundances

T. M. Stanton <sup>1</sup>\* F. Cullen <sup>1</sup> A. C. Carnall,<sup>1</sup> D. Scholte <sup>1</sup> K. Z. Arellano-Córdova <sup>1</sup>  
 D. J. McLeod <sup>1</sup> R. Begley <sup>1</sup> C. T. Donnan <sup>1</sup> J. S. Dunlop,<sup>1</sup> M. L. Hamadouche <sup>2</sup> R. J. McLure,<sup>1</sup>  
 A. E. Shapley,<sup>3</sup> C. Bondestam,<sup>1</sup> and S. Stevenson<sup>1</sup>

<sup>1</sup>*Institute for Astronomy, University of Edinburgh, Royal Observatory, Edinburgh, EH9 3HJ, UK*

<sup>2</sup>*Department of Astronomy, University of Massachusetts, Amherst, MA 01003, USA;*

<sup>3</sup>*Department of Physics & Astronomy, University of California, 430 Portola Plaza, Los Angeles CA 90095, USA*

Accepted XXX. Received YYY; in original form ZZZ

## ABSTRACT

We present an analysis of nine star-forming galaxies with  $\langle z \rangle = 3.95$  from the JWST EXCELS survey for which we obtain robust chemical abundance estimates for the  $\alpha$ -elements O, Ne and Ar. The  $\alpha$ -elements are primarily produced via core-collapse supernovae (CCSNe) which should result in  $\alpha$ -element abundance ratios that do not vary significantly across cosmic time. However, Type Ia supernovae (SNe Ia) models predict an excess production of Ar relative to O and Ne. The Ar/O abundance ratio can therefore be used as a tracer of the relative enrichment of CCSNe and SNe Ia in galaxies. Our sample approximately doubles the number of sources with measurements of Ar/O at  $z > 2$ , and we find that our sample exhibits sub-solar Ar/O ratios on average, with  $\text{Ar/O} = 0.62 \pm 0.10 (\text{Ar/O})_{\odot}$ . In contrast, the average Ne/O abundance is fully consistent with the solar ratio, with  $\text{Ne/O} = 1.07 \pm 0.12 (\text{Ne/O})_{\odot}$ . Our results support a scenario in which Ar has not had time to build up in the interstellar medium of young high-redshift galaxies, which are dominated by CCSNe enrichment. We show that these abundance estimates are in good agreement with recent Milky Way chemical evolution models, and with Ar/O trends observed for planetary nebulae in the Andromeda galaxy. These results highlight the potential for using multiple element abundance ratios to constrain the chemical enrichment pathways of early galaxies with JWST.

**Key words:** galaxies: abundances – galaxies: evolution – galaxies: high redshift

## 1 INTRODUCTION

By tracing the abundances of heavy elements within the interstellar medium (ISM), we can constrain the key secular processes regulating the growth of galaxies, namely the history of star formation and the impact of large-scale inflows and outflows of gas (Maiolino & Mannucci 2019; Péroux & Howk 2020). Measurements of O, the most abundant metal by mass, provide a good proxy for the total metallicity and are readily measurable from bright rest-frame optical lines. These have been used to establish the existence of the gas-phase mass-metallicity relationship (MZR; Tremonti et al. 2004; Erb et al. 2006; Maiolino et al. 2008; Andrews & Martini 2013; Cullen et al. 2014; Sanders et al. 2021; Scholte et al. 2024) and investigate the fundamental metallicity relationship (FMR; Lara-López et al. 2010; Mannucci et al. 2010; Sanders et al. 2021; Curti et al. 2024) from the local Universe out to  $z \approx 10$ .

Further insights can be gained by tracing the relative abundances of different elements (e.g., Kobayashi et al. 2020b). For example, studies at  $z > 2$  have increasingly focused on measurements of the stellar Fe abundance from ultra-deep rest-frame far-ultraviolet

(FUV) data. These analyses have revealed the existence of the stellar MZR at high redshifts (e.g., Cullen et al. 2019; Kashino et al. 2022; Chartab et al. 2024; Stanton et al. 2024). It has also become clear that star-forming galaxies at these redshifts exhibit elevated O/Fe ratios relative to the solar values (i.e.,  $\alpha$ -enhancement), a sign that the interstellar medium (ISM) is enriched predominantly by the products of core-collapse supernovae (CCSNe). This is a direct consequence of the delayed production of iron via Type-Ia supernovae (SNe Ia) - with a typical delay time of  $\approx 1$  Gyr - resulting in an iron-deficient ISM (Kobayashi et al. 2020b). Most recently, in Stanton et al. (2024) we simultaneously measured the O and Fe abundances of 65 star-forming galaxies at  $\langle z \rangle \approx 3.5$ , finding an average enhancement of  $\langle \text{O/Fe} \rangle \approx 2.7 \times (\text{O/Fe})_{\odot}$ , consistent with other measurements across the literature (e.g., Steidel et al. 2016; Topping et al. 2020a,b; Cullen et al. 2021; Kashino et al. 2022; Strom et al. 2022; Chartab et al. 2024).

These  $\alpha$ -enhanced abundances offer a natural explanation for the offset observed between high-redshift and local populations in strong emission-line ratio diagrams (e.g., the BPT diagram; Shapley et al. 2019; Jeong et al. 2020; Clarke et al. 2023; Shapley et al. 2024). For example, an Fe deficit will result in harder stellar ionising spectra at fixed O abundance (e.g., Topping et al. 2020a), thereby increas-

\* E-mail: t.stanton@ed.ac.uk

ing high-ionisation line strengths (e.g. an elevated  $[\text{O III}]/\text{H}\beta$  ratio). Furthermore, in [Stanton et al. \(2024\)](#) we have demonstrated how interpreting the mass-dependence of element abundance ratios such as  $\text{O}/\text{Fe}$  with chemical evolution models (e.g., [Weinberg et al. 2017](#)) can place unique constraints on galaxy-scale outflow efficiencies (see also; [Chartab et al. 2024](#)). Perhaps most intriguingly, abundance ratios such as  $\text{O}/\text{Fe}$  also represent a unique pathway for linking high-redshift galaxies with detailed stellar archaeological measurements of the Milky Way and Local Group (e.g., [Cullen et al. 2021](#), Monty et al. in prep) connecting star formation at high-redshift to descendant populations within our own Galaxy.

Despite their growing number, estimates of Fe abundances at high redshift remain extremely difficult to obtain because of the requirement for rest-frame FUV continuum spectroscopy. Although progress may be made for the brightest sources at extreme redshifts with JWST (e.g., [Nakane et al. 2024](#)), individual Fe determinations will not be possible for large samples of galaxies until the Extremely Large Telescope era. Whilst  $[\text{Fe II}]$  lines are measurable in the rest-frame optical and near-IR, interpreting measurements of these features requires significant dust depletion corrections. However, in lieu of using Fe, other elements with SNe Ia production channels can be used to trace the relative enrichment of SNe Ia and CCSNe at early times. One such promising element is Ar. Although Ar is an  $\alpha$ -element, models predict that  $\approx 34\%$  of the total Ar production is a result of SNe Ia ([Kobayashi et al. 2020a](#)). As a result, the  $\text{O}/\text{Ar}$  ratio can be used as a tracer of the degree of enrichment of CCSNe versus SNe Ia, and, following Fe, one would expect a deficit of Ar with respect to O in high-redshift galaxies.

Indeed, observational evidence for delayed Ar production was recently provided by [Arnaboldi et al. \(2022\)](#), who analysed the abundances of O and Ar in planetary nebulae and  $\text{H II}$  regions within M31 and found an increase in  $\text{O}/\text{Ar}$  towards lower  $\text{Ar}/\text{H}$ . The observed sequence in  $\text{O}/\text{Ar} - \text{Ar}/\text{H}$  displays a striking similarity to the  $\text{O}/\text{Fe} - \text{Fe}/\text{H}$  sequence observed in Milky Way stars. Moreover, a small number of recent studies have demonstrated that it is possible to constrain direct Ar abundances of individual galaxies at high redshift from detections of the  $[\text{Ar III}]\lambda 7135$  and  $[\text{Ar IV}]\lambda 4713, 4741$  emission lines. For example, [Rogers et al. \(2024\)](#) performed a thorough chemical abundance analysis of a  $z \sim 3$  galaxy observed as part of the CECILIA survey ([Strom et al. 2023](#)), finding a sub-solar  $\text{Ar}/\text{O}$  abundance ratio, consistent with a scenario wherein Ar has a significant SNe Ia production channel. In contrast, an analysis by [Welch et al. \(2024\)](#) of the Sunburst Arc (a highly lensed galaxy at  $z \approx 2.37$ ) yielded an  $\text{O}/\text{Ar}$  measurement close to the solar value. Recently, [Bhattacharya et al. \(2024\)](#) have analysed a sample of public-release JWST spectra at  $1.3 < z < 7.7$ , finding  $\text{O}/\text{Ar}$  ratios that are mostly consistent with a combination of CCSNe and SNe Ia production channels.

These early JWST studies clearly demonstrate the potential of using Ar to study the chemical enrichment and star-formation histories of galaxies in the early Universe out to  $z \approx 6$  (beyond which most Ar lines emission features are inaccessible with JWST/NIRSpec). In contrast to Fe, which requires deep stellar continuum observations, Ar abundances can be estimated using emission lines that are readily detected by JWST. However, the sample of high-redshift galaxies with direct Ar abundance determinations remains small, and the current results do not paint an entirely clear picture. A full understanding of the formation channels of Ar, and its potential as a tracer of  $\alpha$ -enhanced abundances at early times, requires larger samples.

In this work, we select a sample of star-forming galaxies from the JWST Early eXtragalactic Continuum and Emission Line Survey (EXCELS; [Carnall et al. 2024](#)) in the redshift range  $1.8 < z < 5.3$ ,

with detections of the emission lines required to directly measure the abundances of O and Ar. Crucially, we are also able to constrain the Ne abundances for our sample using the  $[\text{Ne III}]\lambda 3870$  emission line. As a pure  $\alpha$ -element, the enrichment of Ne is expected to follow O and therefore can be used as a control element. Specifically, we can test the hypothesis that while  $\text{Ne}/\text{O}$  ratios should be consistent with the solar value in high redshift galaxies,  $\text{Ar}/\text{O}$  ratios might show an offset to lower values.

The structure of this paper is as follows. In Section 2, we discuss our sample selection and the EXCELS data set used in this work. The methodologies we employ to measure the abundances of O, Ar and Ne from our spectra are described in Section 3. We present our measured abundance ratios and discuss our results in Section 4. In Section 5, we discuss the effect of systematic uncertainties related to atomic data, ionisation correction factors (ICFs), and dust depletion on our results. Finally, we summarise our conclusions in Section 6.

Throughout this work, metallicities are quoted relative to a solar abundance value taken from [Asplund et al. \(2021\)](#) unless otherwise stated. The key solar abundance values relevant to our analysis are:  $12 + \log(\text{O}/\text{H}) = 8.69$ ,  $12 + \log(\text{Ne}/\text{H}) = 8.06$  and  $12 + \log(\text{Ar}/\text{H}) = 6.38$ . We also adopt the following definition for representing a chemical abundance ratio relative to the solar value:  $[X/Y] = \log(X/Y) - \log(X/Y)_{\odot}$ . We assume the following cosmology:  $\Omega_{\text{M}} = 0.3$ ,  $\Omega_{\Lambda} = 0.7$ , and  $H_0 = 70 \text{ km s}^{-1} \text{ Mpc}^{-1}$ .

## 2 DATA AND SAMPLE PROPERTIES

The primary galaxy sample analysed here is taken from the JWST EXCELS spectroscopic survey (GO 3543; PIs: Carnall, Cullen; [Carnall et al. 2024](#)). The EXCELS survey is designed to provide medium-resolution ( $R = 1000$ ) spectroscopy of targets selected from JWST/PRIMER imaging (GO 1837; PI: Dunlop) in the UDS field. We observe 4 NIRSpec/MSA pointings that are optimised to target rare massive quiescent galaxies at high redshift, with the remaining MSA slitlets allocated to star-forming galaxies in the redshift range  $1 < z < 8$ . Full details of the EXCELS target selection, observing strategy, and data reduction are described in [Carnall et al. \(2024\)](#). Below, we briefly review the observations and data reduction.

### 2.1 Data reduction

Each of the four NIRSpec/MSA pointings is observed with the G140M/F100LP, G235M/F170LP and G395M/F290LP gratings. Observations were conducted using a 3 shutter slitlet and 3-point dither pattern. The total integration times within each grating for each pointing are  $\approx 4$  hours in G140M and G395M, and  $\approx 5.5$  hours in G235M, using the NRSIRS2 readout pattern. As described in [Carnall et al. \(2024\)](#), separate MSA configurations are specified for each grating to maximise the number of objects for which we can observe the key rest-frame UV and optical spectral features. The majority of objects presented in this work have observations in the G235M and G395M gratings which provides coverage of the vital rest-frame optical emission lines at the median redshift of our sample.

To reduce the data, we begin by processing the raw level 1 products from the Mikulski Archive for Space Telescopes (MAST) using v1.15.1 of the JWST reduction pipeline<sup>1</sup>. We run the default level 1 configuration except for turning on advanced snowball rejection and make use of the `CRDS_CTX = jwst_1258.pmap` version of

<sup>1</sup> <https://github.com/spacetelescope/jwst>

the JWST Calibration Reference Data System (CRDS) files. We then run the level 2 pipeline steps assuming the default configuration except for turning off the sky subtraction step. The level 3 pipeline provides the final combined 2D spectra that can be used for science analysis. We then perform our own custom 1D optimal extraction of the 2D spectra (Horne 1986) setting the extraction centroid as the flux-weighted mean position of the object within the NIRSpec/MSA slitlet (see Carnall et al. 2024).

A flux-calibration step is needed to correct for wavelength-dependent slit losses due to the increasing FWHM of the PSF with wavelength. Additionally, small offsets in the source position within the slit can result in flux mismatches between the different gratings. To match the flux level between the different gratings, we calculate the median flux in overlapping wavelength regions and scale the G140M and/or G395M spectra to the G235M spectra.

To achieve the absolute flux calibration we perform a spectrophotometric calibration to the broadband photometry similar to the approach adopted for the CECILIA survey (Rogers et al. 2024). Each galaxy in the EXCELS sample benefits from deep HST and JWST/NIRCam imaging spanning the wavelength range  $0.4 - 5\mu\text{m}$  in 11 photometric bands: F435W, F606W, F814W, F090W, F115W, F150W, F200W, F277W, F356W, F410M and F444W. Broadband fluxes from the PSF-homogenised images are extracted using 0.5 arcsec diameter apertures and corrected to total using the F356W FLUX\_AUTO values measured by SOURCEEXTRACTOR (Bertin & Arnouts 1996). We integrate each EXCELS spectrum through the overlapping filters and scale these to the imaging fluxes. The correction as a function of wavelength is derived via a linear interpolation between the bands. As all of the sources studied in this paper have significant stellar continuum detections (e.g., Fig 1) scaling to the photometry in this way should account for wavelength-dependent slit losses and provide as accurate a flux calibration as is possible. Applying this method to the four quiescent galaxies presented in Carnall et al. (2024) we find that the flux calibration is accurate to within  $\lesssim 5$  per cent<sup>2</sup>.

## 2.2 Sample Selection

To achieve our science goals we require detections of all of the emission lines necessary for a direct determination of O, Ar and Ne abundances. From the full EXCELS sample of star-forming galaxies, we select galaxies with  $S/N > 2$  detections of:

- (i) The [O III] $\lambda$ 5007, [O III] $\lambda$ 4363 emission lines necessary to directly measure the electron temperature ( $T_e$  [O III]) and the total oxygen abundance ( $12 + \log(\text{O}/\text{H})$ )
- (ii) The [Ar III] $\lambda$ 7135 emission line required to determine Ar/H
- (iii) At least two Balmer emission lines (i.e., H  $\alpha$ , H  $\beta$ , H  $\gamma$ , H  $\delta$ ) which we need to perform robust nebular reddening corrections.

As our primary abundance ratio of interest is Ar/O, we do not require the detection of [Ne III] $\lambda$ 3870 for inclusion into our sample, however all but one of our galaxies also exhibit this line.

From an initial sample of eleven, we find two galaxies display H  $\alpha$ /H  $\beta$  ratios which are lower than the theoretical ratios from Case

B recombination theory with a significance of  $\geq 2\sigma$ . Deviations from Case B recombination ratios have been observed in a number of high-redshift galaxy spectra, and have been attributed to gas geometry and optical thickness to H  $\alpha$  photons (e.g., Scarlata et al. 2024), or alternatively to density bounded nebulae (McClymont et al. 2024). Due to the increased uncertainty in modelling the ionization conditions and reddening corrections for these galaxies, we exclude them from our final sample. Our final sample therefore comprises of nine galaxies across a redshift range  $1.8 < z < 5.3$ . This sample represents a significant increase in the number of galaxies with direct Ar/O determinations at high redshift. An example galaxy from our final sample (EXCELS-40081) is shown in Figure 1.

## 2.3 Measurements and derived quantities

### 2.3.1 Fitting emission-line profiles

The emission line fluxes are measured using a two step approach where first the continuum flux is subtracted and following that all emission lines are fitted using Gaussian line profiles. The continuum flux is measured using the running mean value of the 16<sup>th</sup> to 84<sup>th</sup> percentile flux values within a top hat function with a rest-wavelength width of 350 Å. We use the continuum-subtracted residuals to re-estimate the flux uncertainties returned by the analysis pipeline. We do this by a multiplication factor such that  $\tilde{\sigma}_F = \frac{1}{2}(R_{84} - R_{16})$ , where  $\tilde{\sigma}_F$  is the median flux uncertainty and  $R_{16}$ ,  $R_{84}$  are the 16<sup>th</sup>, 84<sup>th</sup> percentiles of the residuals. We find error multiplication factors in the range  $\tilde{\sigma}_F \simeq 1.5 - 2$ , in good agreement with independent analyses (Maseda et al. 2023; Carnall et al. 2024). We fit the emission lines to the continuum subtracted residuals with re-estimated uncertainties using Gaussian line profiles. All of the emission lines are fit simultaneously using a common intrinsic line width and line velocity, and the line amplitude is freely fitted for each emission line. The total width of an emission line,  $\sigma_{\text{tot}}$ , is a convolution of intrinsic broadening as well as instrumental broadening which is dependent on the line wavelength and the NIRSpec grating used:  $\sigma_{\text{tot}}^2 = \sigma_{\text{intrinsic}}^2 + \sigma_{\text{grating}}^2(\lambda)$ . The  $\chi^2$ -minimisation is performed with the SciPy least squares implementation (Branch et al. 1999; Virtanen et al. 2020). The emission line flux uncertainties are calculated using a line-profile weighted average of the pixel flux uncertainties (e.g., Moustakas et al. 2023). A full description of our emission line fitting method will be outlined in Scholte et al. (in prep).

### 2.3.2 Measuring stellar masses and star-formation rates

To determine the masses and star-formation rates (SFRs) of our galaxies, we employ spectral energy distribution (SED) fitting to the broadband photometry of our galaxies. Each galaxy has full PRIMER imaging coverage from  $\lambda_{\text{obs}} = 0.4 - 5.0\mu\text{m}$ , with approximately half of the sources having additional detections in the MIRI/F770W filter.

We fit the broadband photometry with BAGPIPES (Carnall et al. 2018) to determine the best-fitting SEDs, and the corresponding stellar masses and SFRs. We perform emission-line corrections to the photometry and fit only the stellar SED component. We fit with the Bruzual & Charlot (2003) models, and assume a flexible dust attenuation law following Salim et al. (2018) and a double power-law star-formation history with a Kroupa (2001) initial mass function (IMF). Full details of the BAGPIPES fitting for the EXCELS star-forming sample will be given in Scholte et al. (in prep.).

The best-fitting stellar masses and star-formation rates (SFRs) and their associated uncertainties are calculated by taking the 16<sup>th</sup>, 50<sup>th</sup>

<sup>2</sup> These quiescent galaxies benefit from high S/N continuum detections and well-understood continuum properties. This enables more accurate flux calibrations to be performed via comparisons to empirical spectral templates as described in Carnall et al. (2024). Our cruder approach (i.e., a simple spectro-photometric scaling) yields fluxes accurate to within  $\simeq 5$  per cent of this method.

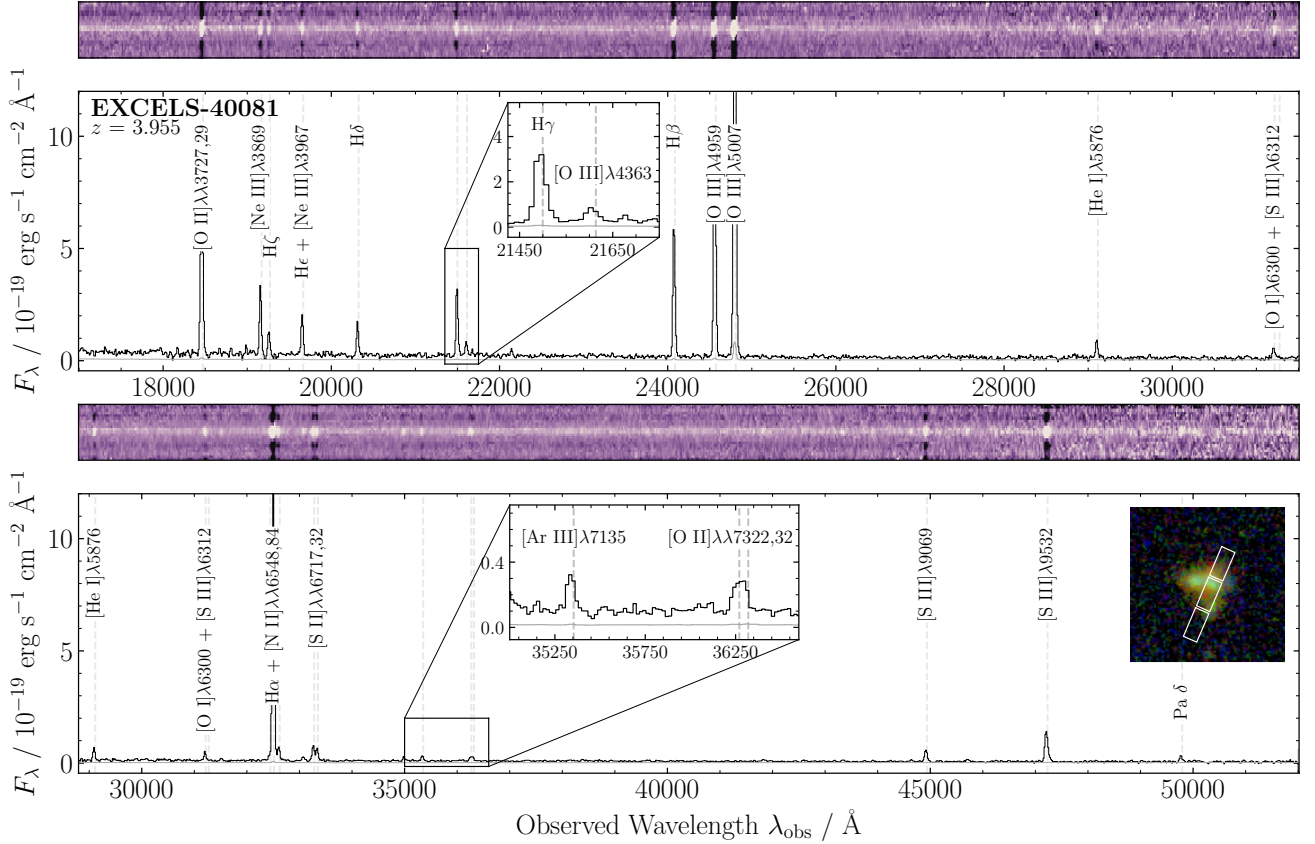


**Figure 1.** An example of one galaxy from our sample (EXCELS-40081,  $z = 3.955$ ) which features all of the required emission lines needed to determine the Ar/O and Ne/O abundance ratios. The top two panels show the NIRSpec/G235M 2D and 1D spectra of this source, and the bottom two panels show the same for NIRSpec/G395M. Prominent emission lines are labelled in each 1D spectrum. Within the NIRSpec/G235M 1D panel, the inset panels show the [O III]  $\lambda 4363$  auroral emission line used to derive the [O III] region electron temperature that is needed for robust element abundance estimates. Similarly in the NIRSpec/G235M 1D panel, the inset panel shows the [Ar III]  $\lambda 7135$  line which we use to determine Ar abundances. In the upper right-hand corner of the bottom panel, we show a false three-colour image of EXCELS-40081 generated from the F115W+F150W, F200W+F277W and F356W+F444W PRIMER imaging with the NIRSpec/MSA slitlets overlotted in white.

**Table 1.** The IDs, redshifts, coordinates, masses and star-formation rates of the nine selected EXCELS star-forming galaxies. The median redshift of the sample is  $\langle z \rangle \approx 3.95$ . Stellar masses and SED-based star-formation rates are derived from fitting the emission-line corrected broad-band photometry with BAGPIPES (Carnall et al. 2018).  $E(B - V)$  values and  $H\alpha$ -based SFRs are measured as described in Sections 2.3.3 and 2.4.

EXCELS ID	RA	DEC	$z_{\text{spec}}$	$\log(M_{\star}/M_{\odot})$	$\log(\text{SFR}_{\text{SED}}/M_{\odot}\text{yr}^{-1})$	$\log(\text{SFR}_{H\alpha}/M_{\odot}\text{yr}^{-1})$	$E(B - V)$
EXCELS-40081	34.3659	-5.2608	3.954	$9.07^{+0.10}_{-0.09}$	$1.52^{+0.14}_{-0.12}$	$1.78 \pm 0.11$	$0.05 \pm 0.07$
EXCELS-45052	34.3671	-5.2520	4.234	$9.69^{+0.05}_{-0.05}$	$2.08^{+0.12}_{-0.11}$	$1.55 \pm 0.14$	$0.32 \pm 0.10$
EXCELS-45177	34.3632	-5.2523	2.901	$8.28^{+0.05}_{-0.06}$	$1.21^{+0.08}_{-0.08}$	$1.02 \pm 0.09$	$0.12 \pm 0.03$
EXCELS-47143	34.2622	-5.2489	3.233	$8.76^{+0.09}_{-0.12}$	$0.88^{+0.26}_{-0.35}$	$0.84 \pm 0.10$	$0.14 \pm 0.03$
EXCELS-52422	34.2503	-5.2406	4.025	$8.12^{+0.08}_{-0.08}$	$0.73^{+0.11}_{-0.11}$	$1.17 \pm 0.10$	$0.07 \pm 0.06$
EXCELS-52712	34.3762	-5.2401	3.238	$8.71^{+0.29}_{-0.04}$	$1.63^{+0.09}_{-0.07}$	$1.35 \pm 0.09$	$0.16 \pm 0.03$
EXCELS-59720	34.3797	-5.2282	4.367	$9.31^{+0.10}_{-0.11}$	$1.22^{+0.12}_{-0.10}$	$1.15 \pm 0.09$	$0.00 \pm 0.03$
EXCELS-94335	34.2728	-5.1717	1.812	$8.95^{+0.07}_{-0.05}$	$1.63^{+0.13}_{-0.19}$	$1.19 \pm 0.09$	$0.22 \pm 0.01$
EXCELS-121806	34.4039	-5.1304	5.226	$8.11^{+0.09}_{-0.05}$	$1.07^{+0.08}_{-0.07}$	$1.25 \pm 0.09$	$0.01 \pm 0.04$

and 84<sup>th</sup> percentiles of their respective resulting posterior distributions. For the SFRs, we adopt values averaged over the last 10 Myr of the star-formation history. The coordinates, redshifts, stellar masses and SED-based SFRs of our final sample are summarised in Table 1. For each galaxy, we measure the underlying stellar absorption of the Balmer lines from the best-fitting SED and correct our measured emission line fluxes for this absorption. These corrections result in median increases of  $\lesssim 1$  per cent to the observed emission-line fluxes for the main Balmer lines used this study ( $H\alpha$  and  $H\beta$ ).

### 2.3.3 Reddening corrections for nebular line fluxes

In each of our galaxies we detect  $H\alpha$  and  $H\beta$ , with additional detections of  $H\gamma$  and  $H\delta$  in some galaxies, and use the ratios of these lines to correct our observed emission-line fluxes for the effects of nebular dust reddening<sup>3</sup>. For each Balmer line ratio, we calculate the theoretically expected line value from Storey & Hummer (1995) assuming case B recombination with  $T_e = 12,000$  K and  $n_e = 300$  cm<sup>-3</sup>. These values are chosen as the approximate average values measured across our sample. To calculate  $E(B - V)_{\text{neb}}$  we take the weighted average across all Balmer ratios assuming the Cardelli et al. (1989) extinction curve. We note that although the Cardelli et al. (1989) curve has been shown to be a good approximation of the nebular attenuation law in high-redshift star-forming galaxies (e.g. Reddy et al. 2020), a recent detailed analysis of a deep galaxy spectrum at  $z = 4.41$  has demonstrated that the true attenuation law is likely to vary on a galaxy-by-galaxy basis (Sanders et al. 2024). We lack the dynamic range in wavelength to accurately derive the dust curve for each of our objects individually, and therefore adopt the Cardelli et al. (1989) relation as representative of the typical attenuation curve at these redshifts. To estimate the uncertainties, we perturb the line ratios by their associated errors 500 times and recalculate  $E(B - V)_{\text{neb}}$ , taking the median and standard deviation of the resulting distributions. The final values and uncertainties are reported in Table 1. We use this final value of  $E(B - V)_{\text{neb}}$  to dust-correct all of our observed line fluxes.

## 2.4 $H\alpha$ star-formation rates and the relation to the star-forming main sequence

We convert our dust-corrected  $H\alpha$  line luminosities into SFRs using the conversion of Hao et al. (2011) for a Kroupa (2001) IMF<sup>4</sup>. The bottom panel of Fig. 2 shows the comparison between the  $H\alpha$ - and SED-derived SFRs, where it can be seen that there is good agreement. Taking into consideration the various systematic uncertainties and SED modelling assumptions (not included in Fig. 2) we consider both estimates to be fully consistent. Assuming either SFR estimate, it is clear that the galaxies in our sample are highly star forming, with SFRs  $\gtrsim 10 M_{\odot}\text{yr}^{-1}$ .

In the upper panel of Fig. 2, we show the positions of our sample with respect to star-forming main sequence at  $z \simeq 4 - 5$  (taken from Speagle et al. 2014 and Clarke et al. 2024). It can be seen that the galaxies presented here sit primarily above the main sequence,

<sup>3</sup> For some galaxies we also detect lower order Balmer lines (e.g.,  $H\epsilon$  and  $H\eta$ ), however, as these lines are contaminated by nearby emission lines, we do not include them in our nebular reddening calculation.

<sup>4</sup> This conversion is chosen to maintain consistency with our SED modelling assumptions, though we note that other conversion factors tuned to sub-solar metallicities will return lower SFR $_{H\alpha}$  (e.g., Clarke et al. 2024), and as such our SFRs may be overestimated.

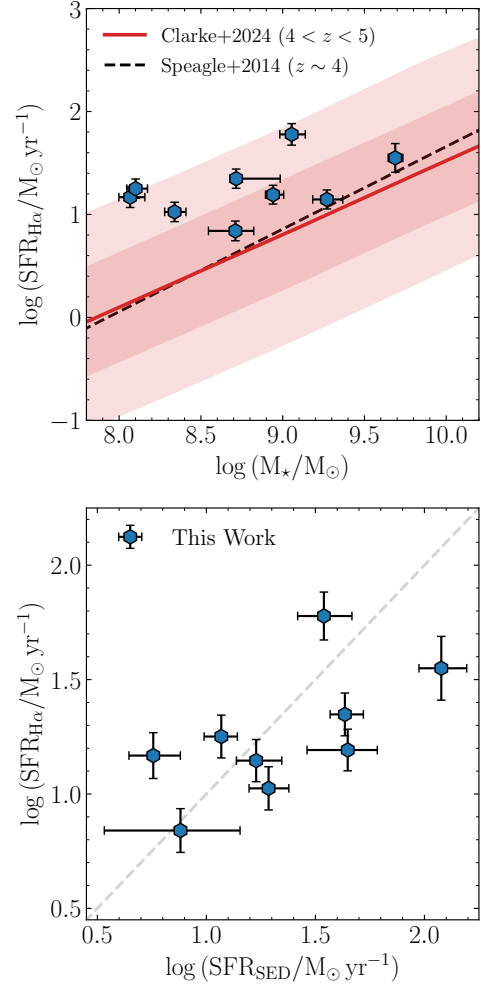


**Figure 2.** The top panel shows the star-forming main sequence for our sample (hexagons). The star-formation rates are derived from dust-corrected  $H\alpha$  luminosities assuming the Hao et al. (2011) conversion. For comparison, we plot the star-forming main sequence relations from Speagle et al. (2014) at  $z = 4$  (dashed black line) and from Clarke et al. (2024) at  $4 < z < 5$  (red line). The shaded red regions highlight the  $1\sigma$  and  $2\sigma$  intrinsic scatter intervals about the Clarke et al. (2024) relation. The bottom panel shows a comparison between the  $H\alpha$ - and SED-derived SFRs. The sample is generally scattered around the unity line (grey dashed) indicating that our SED fitting is accurately capturing the star-formation properties of the sample. Assuming either SFR estimate, it is clear that our sample consists of galaxies with above-average SFRs at  $z \simeq 4$  (i.e., SFRs  $\gtrsim 10 M_{\odot}\text{yr}^{-1}$ ).

although all fall approximately within the  $2\sigma$  intrinsic scatter of the Clarke et al. (2024) relation. This is the case regardless of whether we assume  $H\alpha$ - or SED-based SFRs. Therefore, we note that the results presented below are primarily applicable to the galaxies with above-average SFRs at  $z \simeq 4$ , although it is worth pointing out that 4 galaxies in our sample fall on, or within  $1\sigma$  of, the main sequence.

## 3 DETERMINING PHYSICAL CONDITIONS AND ABUNDANCES

In order to measure the chemical abundances of our galaxies we first characterise their temperature and density structures. We assume

**Table 2.** The atomic data utilised in this work.

Ion	Transition Probabilities ( $A_{ij}$ )	Collision Strengths ( $\Upsilon_{ij}$ )
O <sup>+</sup>	Froese Fischer & Tachiev (2004)	Kisielius et al. (2009)
O <sup>2+</sup>	Froese Fischer & Tachiev (2004)	Storey, Sochi & Badnell (2014)
Ne <sup>2+</sup>	Froese Fischer & Tachiev (2004)	McLaughlin et al. (2011)
S <sup>+</sup>	Irimia & Froese Fischer (2005)	Tayal & Zatsarimny (2010)
Ar <sup>2+</sup>	Mendoza & Zeippen (1983)	Munoz Burgos et al. (2009)

a three-zone structure, comprising low-, intermediate-, and high-ionization zones (e.g., Berg et al. 2021). We do not consider a fourth ‘very high’ ionization zone because we do not significantly detect any ionic species corresponding to this zone. We attribute each ionic species to an ionization zone on the basis of its ionization potential (IP). The low ionization zone comprises O<sup>+</sup> and S<sup>+</sup>, which have IPs of 13.6 eV and 10.4 eV respectively. The ions Ar<sup>2+</sup> and S<sup>2+</sup>, which have IPs of 27.6 eV and 23.3 eV, are classified in the intermediate ionization zone. Finally, the high ionization zone contains O<sup>2+</sup> and Ne<sup>2+</sup>, which have ionization potentials of 35.1 eV and 41.0 eV.

### 3.1 Temperature structure

To determine electron temperatures, densities and ionic abundances we use the PYNEB package (v1.1.18; Luridiana et al. 2015), adopting the atomic data listed in Table 2. For each of our galaxies, we estimate the temperature of the high-ionization zone using the [O III] $\lambda$ 4363/[O III] $\lambda$ 5007 ratio. As there are no instances where we have a S/N > 2 detection of the auroral [S II] $\lambda$ 6312 emission line, we calculate the temperature of the intermediate ionization zone using the  $T_e$ [O III]- $T_e$ [S III] scaling relation of Garnett (1992), defined as

$$T_e[\text{S III}] = 0.83 \times T_e[\text{O III}] + 1700 \text{ K}, \quad (1)$$

to which we add an uncertainty of 1300 K in quadrature to account for the scatter of the relation (Rogers et al. 2021). Although we have a few significant detections of the [O II] $\lambda$ 7322, 7332 line, for these sources we measure  $T_e$ [O II] >>  $T_e$ [O III] which is unphysical. The overestimated  $T_e$ [O II] can be attributed to the high sensitivity of the [O II] $\lambda$ 7322, 7332/[O II] $\lambda$ 3726, 3729 ratio to reddening corrections, flux calibration and density fluctuations (e.g., Méndez-Delgado et al. 2023). Therefore, to ensure consistency for the full sample we use the  $T_e$ [O III]- $T_e$ [O II] scaling relationship of Campbell et al. (1986), defined as

$$T_e[\text{O II}] = 0.7 \times T_e[\text{O III}] + 3000 \text{ K}, \quad (2)$$

to measure the temperature of the low ionization zone, to which we add an additional uncertainty of 1100 K (Rogers et al. 2021).

### 3.2 Electron density

Estimates of the electron densities ( $n_e$ ) across the different ionization zones require measurements of emission-line doublets of the same ionic species, namely the [S II] $\lambda$ 6717, 6731 and [O II] $\lambda$ 3726, 3729 doublets for the low-ionization zone and the [Ar IV] $\lambda$ 4713, 4741 doublet for the high-ionization zone (e.g., Minozzi et al. 2022). We use [S II] $\lambda$ 6717/[S II] $\lambda$ 6731 as our density diagnostic as [O II] $\lambda$ 3726, 3729 is unresolved at the resolution of our data and we do not detect [Ar IV] $\lambda$ 4713, 4741 in any of our galaxies.

We assume a uniform density structure and use the  $n_e$ [S II] estimate to calculate all ionic abundances. In general, this should not have a strong effect on our results. The Ar<sup>2+</sup> and O<sup>2+</sup> abundances are essentially insensitive to  $n_e$  within the range  $10^2 < n_e < 10^4 \text{ cm}^{-3}$ , changing by  $\lesssim 0.001$  dex and  $\lesssim 0.005$  dex respectively. The O<sup>+</sup> abundance is more sensitive to density, increasing significantly with density above  $n_e \simeq 10^{3.5} \text{ cm}^{-3}$  (below this limit, the ionic abundance varies by  $\lesssim 0.02$  dex, which is less than the uncertainty on a given oxygen abundance). However, this should not be a significant issue since our sample exhibits high [O III]/[O II] ratios (i.e.,  $\log([\text{O III}]\lambda 5007/[\text{O II}]\lambda 3726, 3729) = 0.5 \pm 0.2$ ) typical of high-redshift galaxies, indicating that O<sup>2+</sup> dominates the total O abundance (e.g., Shapley et al. 2024). Moreover, electron densities of  $n_e > 10^{3.5} \text{ cm}^{-3}$  are rare at the redshifts of our sample, and are instead typically within the range 100 – 500  $\text{cm}^{-3}$  (e.g. Isobe et al. 2023a).

In cases where the density is unconstrained (i.e., the [S II] $\lambda$ 6717, 6731 emission lines are not significantly detected), we assume a fixed  $n_e = 300 \text{ cm}^{-3}$ ; this value is also broadly consistent with the weighted average value we determine from the EXCELS galaxies with  $n_e$  constraints of  $\simeq 300 \text{ cm}^{-3}$  (see Table 3).

### 3.3 Ionic and total abundances

We calculate the ionic abundances for each of our desired ionic species using the integrated line fluxes, the temperature corresponding to their ionization zone and the electron density. To account for uncertainties in the temperatures, densities and emission line strengths, we perturb each parameter by its associated error 500 times and re-calculate the abundances. The resulting ionic abundances and their uncertainties are given by the median and scaled median absolute deviation of the resulting distribution.

Typically, the only observed ionization states of oxygen are O<sup>+</sup> and O<sup>2+</sup>, with a negligible amount of oxygen in the O<sup>3+</sup> state (e.g., Berg et al. 2021). Therefore, the total oxygen abundance is simply sum the ionic abundances corresponding to O<sup>+</sup> and O<sup>2+</sup>:

$$\frac{\text{O}}{\text{H}} = \frac{\text{O}^+}{\text{H}^+} + \frac{\text{O}^{2+}}{\text{H}^+}. \quad (3)$$

However, this is not the case for all elements of interest. For example, we only observe the Ar<sup>2+</sup> state of argon, and there are non-negligible contributions from Ar<sup>+</sup> and Ar<sup>3+</sup><sup>5</sup>. Similarly, we only observe the Ne<sup>2+</sup> state of neon. To account for the unseen ions and infer the total abundance of these elements we employ an ionization correction factor (ICF) such that:

$$\frac{\text{X}}{\text{H}} = \frac{\text{X}^{2+}}{\text{H}^+} \times \text{ICF}(\text{X}^{2+}). \quad (4)$$

From the variety of available ICFs, we use the ICFs of Izotov et al. (2006) which are derived from photoionization modelling and incorporate dependencies on ionization parameter and metallicity. These ICFs have been shown to be suitable for high-redshift analogue galaxies (e.g., Arellano-Córdova et al. 2024) and, as such, should be appropriate for our high-redshift sample. We discuss the systematic uncertainties related to our choice of ICFs in Section 5.1.

<sup>5</sup> Whilst we have spectral coverage of [Ar IV] $\lambda$ 4713, 4741, we have no significant detections of this feature in any of our galaxies. We note that including [Ar IV] in the determination of Ar abundances typically results in differences of  $\log(\text{Ar}/\text{O}) \lesssim 0.05$  dex (Arellano-Córdova et al. 2024), which is well within our uncertainties on our measured abundances.

**Table 3.** The temperatures, densities, and O/H, Ne/O and Ar/O abundance ratios for our sample. All  $T_e$  [S III] and  $T_e$  [O II] value are estimated from  $T_e$  [O III] using equations 1 and 2 respectively. The O abundances are uncorrected for dust depletion, as discussed in Section 5.2.

EXCELS ID	$T_e$ [O III] / K	$T_e$ [S III] / K	$T_e$ [O II] / K	$n_e$ [S II] / $\text{cm}^{-3}$	$12 + \log(\text{O}/\text{H})$	$\log(\text{Ne}/\text{O})$	$\log(\text{Ar}/\text{O})$
EXCELS-40081	$13600 \pm 1700$	$13000 \pm 1800$	$12500 \pm 1800$	$254 \pm 161$	$7.99 \pm 0.15$	$-0.61 \pm 0.18$	$-2.56 \pm 0.24$
EXCELS-45052	$11300 \pm 2400$	$11100 \pm 2300$	$10900 \pm 2100$	$471 \pm 347$	$8.38 \pm 0.30$	$-0.57 \pm 0.36$	$-2.77 \pm 0.45$
EXCELS-45177	$14100 \pm 1500$	$13400 \pm 1700$	$12900 \pm 1700$	$659 \pm 255$	$8.10 \pm 0.13$	$-0.63 \pm 0.13$	$-2.50 \pm 0.19$
EXCELS-47143	$13000 \pm 2300$	$12500 \pm 2200$	$12100 \pm 2100$	$290 \pm 171$	$8.18 \pm 0.23$	$-0.62 \pm 0.21$	$-2.64 \pm 0.27$
EXCELS-52422	$19700 \pm 2700$	$18100 \pm 2500$	$16800 \pm 2300$	$300^a$	$7.53 \pm 0.13$	$-0.59 \pm 0.16$	$-2.51 \pm 0.24$
EXCELS-52712	$10500 \pm 1800$	$10400 \pm 1800$	$10400 \pm 1800$	$876 \pm 352$	$8.50 \pm 0.25$	— <sup>b</sup>	$-2.86 \pm 0.29$
EXCELS-59720	$12500 \pm 1500$	$12100 \pm 1700$	$11700 \pm 1700$	$970 \pm 376$	$8.13 \pm 0.15$	$-0.63 \pm 0.12$	$-2.49 \pm 0.26$
EXCELS-94335	$11400 \pm 800$	$11100 \pm 1300$	$11000 \pm 1400$	$339 \pm 97$	$8.24 \pm 0.12$	$-0.61 \pm 0.10$	$-2.54 \pm 0.18$
EXCELS-121806	$14900 \pm 1300$	$14100 \pm 1600$	$13400 \pm 1600$	$449 \pm 365$	$7.95 \pm 0.10$	$-0.55 \pm 0.09$	$-2.30 \pm 0.17$

<sup>a</sup> The density of EXCELS-52422 is not constrained as we do not detect the [S II] doublet, for this source we assume a fixed density of  $300 \text{ cm}^{-3}$  (see Section 3)

<sup>b</sup> EXCELS-52712 lacks spectral coverage of [Ne III] $\lambda$ 3870 and therefore no estimate for Ne/O.

## 4 THE ABUNDANCE PATTERNS OF EXCELS GALAXIES

In the following section, we present the Ar/O and Ne/O abundance ratios of our  $1.8 < z < 5.3$  sample and interpret these results in the context of the contributions of CCSNe and SNe Ia. All relevant values of temperature, density, and element abundance are reported in Table 3.

### 4.1 Argon

In Fig. 3 we show our measured Ar/O abundances as a function of redshift and compare to other literature results at  $z > 2$ . All data points are derived from JWST/NIRSpec observations with a robust estimate of the electron temperature. It can be seen from our Fig. 3 that our new sample approximately doubles the number of galaxies with Ar/O estimates at these redshifts. Fig. 3 also highlights the capability of moderately deep JWST spectroscopy ( $\simeq 2 - 5$  hours integration time) to deliver Ar/O abundance estimates in the redshift range  $2 < z < 6$ . Future spectroscopic campaigns can significantly increase the number of such measurements and continue to build on the results presented here.

All but one galaxy in our EXCELS sample, and the majority of other literature measurements, fall below the solar Ar/O value (Isobe et al. 2023b; Rogers et al. 2024; Bhattacharya et al. 2024). A notable exception is the Sunburst Arc ( $z = 2.37$ ), which shows an approximately solar ratio with a relatively small uncertainty (Welch et al. 2024). However, it is clear that the average of all current estimates indicates an Ar deficit in high-redshift star-forming galaxies, which we discuss further below. It is perhaps interesting to note that all three current measurements at  $z \gtrsim 5$  are consistent with solar or super-solar Ar/O, which some authors have attributed to exotic enrichment sources at very early times (Watanabe et al. 2024; Bhattacharya et al. 2024). The one  $z > 5$  galaxy in our sample (EXCELS-121806,  $\log(M_\star/M_\odot) = 8.11$ ) has - perhaps by chance - the largest value of Ar/O, and is consistent with the trend seen in other data. The sample size at these redshifts is obviously too small to draw any firm conclusions (one of the three estimates is also an upper limit) but more observations in this redshift regime are clearly of interest, especially given evidence for other anomalous abundance ratios at similar redshifts (e.g. N/O; Topping et al. 2024).

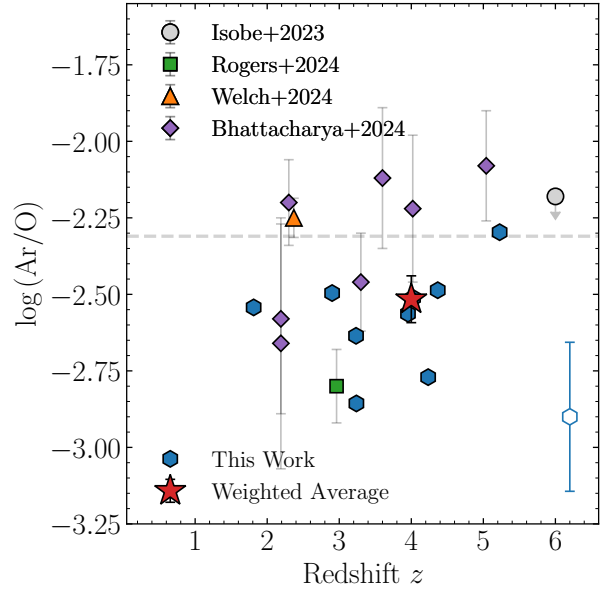


**Figure 3.** The  $\log(\text{Ar}/\text{O})$  abundance as a function of redshift for our sample (blue hexagons) compared other to high-redshift samples from the literature. We show the median average error bar in with an unfilled blue hexagon in the bottom right. The weighted average of our measurements is  $\log(\text{Ar}/\text{O}) = -2.52 \pm 0.07$  and is shown with a red star at the median redshift of the sample ( $z = 3.95$ ). For comparison, we show the measurements of Bhattacharya et al. (2024) (purple diamonds), Rogers et al. (2024) (green square) and Welch et al. (2024) (orange triangle). We additionally plot an upper limit on  $\log(\text{Ar}/\text{O})$  for a  $z \simeq 6$  galaxy with an electron temperature measurement from Isobe et al. (2023b). We denote the solar ratio,  $\log(\text{Ar}/\text{O})_\odot = -2.31$ , with a grey dashed line. The bulk of high-redshift measurements exhibit subsolar  $\log(\text{Ar}/\text{O})$  ratios, indicating a deficiency in Ar enrichment in high-redshift star-forming galaxies.

#### 4.1.1 The metallicity dependence of Ar/O

In Fig. 4, we show how the Ar/O ratio varies as a function of O/H (a proxy for total metallicity) in our sample. Alongside the high-redshift galaxy data, we also include a comparison to a selection of local data comprised of star-forming galaxies from the COS Legacy Archival

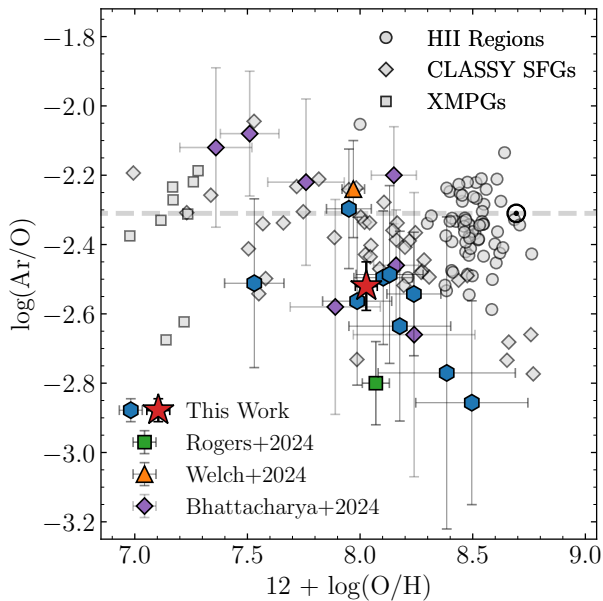


**Figure 4.** The Ar/O ratio as a function of O/H for the EXCELS galaxies (blue hexagons). We compare to other high-redshift systems with reported Ar/O and O/H ratios using the same symbols as Fig. 3. In grey we show measurements from local H II regions (circles; Rogers et al. 2022), extremely metal poor local galaxies from DESI (squares; Zinchenko et al. 2024), and local analogues of high-redshift galaxies from CLASSY (diamonds; Arellano-Córdova et al. 2024). The solar value is denoted with the solar symbol and the solar  $(\text{Ar}/\text{O})_{\odot}$  ratio with a grey dashed line. The bulk of our sample lie below the solar  $\log(\text{Ar}/\text{O})_{\odot}$  value and the local comparison sample. This suggests a deficiency of Ar with respect to O in high redshift systems. The weighted average of the EXCELS galaxies (red star) shows a  $\approx 4\sigma$  offset from the solar value (such that  $\text{Ar}/\text{O} = 0.62 \pm 0.10 (\text{Ar}/\text{O})_{\odot}$ ). These results indicate that the Ar/O ratio is sensitive to the star formation history.

Spectroscopic SurveY (CLASSY; Berg et al. 2022; James et al. 2022; Arellano-Córdova et al. 2024) at  $0.02 < z < 0.18$ , extremely metal-poor galaxies from the early data release of the Dark Energy Spectroscopic Instrument (DESI) at  $0.02 < z < 0.21$  (Zinchenko et al. 2024), and extragalactic H II regions in M33 from Rogers et al. (2022).

The consensus of the local studies is that the Ar/O ratio remains approximately constant and consistent with the solar value at all O/H, suggesting that the Ar/O ratio is insensitive to the history of star formation. Despite the metal-poor nature and low-stellar mass of some of these local sources, it is plausible that there has been enough time for SNe Ia enrichment which would serve to increase Ar/O. For example, local dwarf galaxies and low-mass systems are known to exhibit less  $\alpha$ -enhancement (i.e., be more enriched in SNe Ia products) at fixed metallicity compared to stars in the Milky Way (e.g. the SMC; Mucciarelli et al. 2023).

In contrast to local samples, our EXCELS sample appears to be systematically offset to lower Ar/O at fixed O/H. Although it is clear that the uncertainties on the individual measurements are large, the weighted average of the sample is  $\langle \log(\text{Ar}/\text{O}) \rangle = -2.52 \pm 0.07$  at  $(12 + \log(\text{O}/\text{H})) = 8.03 \pm 0.05$ , representing a  $\approx 3\sigma$  deviation below the solar value. Our results are consistent with the  $z \approx 3$  galaxy presented in Rogers et al. (2024) which also shows a significant deviation to low Ar/O.

The other (albeit limited) high-redshift data show more mixed results, in particular the solar-like Ar/O derived from deep JWST/NIRSpec data of the Sunburst Arc ( $z = 2.37$ ; Welch et al. 2024). However, we note that this galaxy shares a number of properties similar to our highest Ar/O source EXCELS-121806 ( $z = 5.226$ ;  $\log(\text{Ar}/\text{O}) = -2.30 \pm 0.17$ ) including its total metallicity and evidence of enhanced N abundance (discussed in a companion paper; Arellano-Córdova et al. in prep). This could suggest that high Ar/O values in fact represent outliers in the high-redshift population related to enrichment scenarios that are not yet fully understood, but much larger samples are needed before this can be robustly addressed. The larger Ar/O derived by Welch et al. (2024) may also be related to systematic uncertainties in the temperature structure of high-redshift H II regions, which we discuss further in Section 5.3.

The Bhattacharya et al. (2024) sample shows no strong evidence for systematically lower Ar/O, however, we note that their estimates are derived from much shallower data compared to all other high-redshift samples (for example, Isobe et al. (2023b) have reported upper limits for a number of the Bhattacharya et al. (2024) sources). Overall, the data presented here suggests that the Ar/O ratios of high-redshift galaxies are most likely sub-solar, consistent with expectations if Ar has significant SNe Ia production pathway. This is in contrast to local systems, which generally show higher, solar-like Ar/O. In the following section, we will discuss these results in more detail via a comparison to a state-of-the-art chemical evolution model.

Finally, we note that two galaxies in our sample, EXCELS-45052 and EXCELS-94335, show highly sub-solar Ar/O ratios ( $\log(\text{Ar}/\text{O}) \lesssim -2.8$ ). Both galaxies are metal-enriched, with  $12 + \log(\text{O}/\text{H}) = 8.38 \pm 0.30$  and  $8.50 \pm 0.25$  respectively. These metallicities fall within the ‘high-metallicity’ regime ( $12 + \log(\text{O}/\text{H}) \geq 8.2$ ) within which the Ar ICF has been observed to have a strong metallicity dependence and large dispersion of  $\approx 0.16$  dex (Arellano-Córdova et al. 2024). Therefore, it is possible these significantly sub-solar Ar/O ratios are an artefact of an unreliable ICF at high metallicity. Further investigation of the Ar ICFs are required to fully address this issue. The high metallicity of these systems could also be affected by more significant depletion of O onto dust grains, which would also act to reduce the observed Ar/O ratio. We discuss these systematics more thoroughly in Section 5.2. However, we note that, given their significant uncertainties, these two galaxies do not strongly bias the weighted average of our sample.

#### 4.1.2 A comparison to chemical evolution models and inferences from M31 planetary nebulae

In the left-hand panel of Fig. 5 we compare our results to the Milky Way chemical evolution model of Kobayashi et al. (2020b). Here, we adopt the local Universe convention of plotting the ratio a CCSNe element to an SNe Ia element (i.e.,  $[\text{O}/\text{Ar}]$ ) as a function of the abundance of the SNe Ia element (i.e.,  $[\text{Ar}/\text{H}]$ ), where the square brackets denote ratios relative to the solar value. This framing is directly analogous to the  $[\text{Fe}/\text{H}] - [\text{O}/\text{Fe}]$  diagram which has previously been employed in studies of  $\alpha$ -enhancement in high-redshift galaxies (e.g. Cullen et al. 2021; Kashino et al. 2022; Chartab et al. 2024; Stanton et al. 2024).

The Kobayashi et al. (2020b) model (dashed line in Fig. 5) can be interpreted as a temporal relation, with the plateau at  $[\text{Ar}/\text{H}] \lesssim -1.0$  corresponding to CCSNe-dominated yields at early times, the ‘knee’ at  $[\text{Ar}/\text{H}] \approx -1.0$  corresponding to the onset of SNe Ia, and the decline at  $[\text{Ar}/\text{H}] \gtrsim -1.0$  corresponding to the steady build up of SNe Ia products at late times. It can be seen that the EXCELS sample, and most other high-redshift sources, are in good agreement with



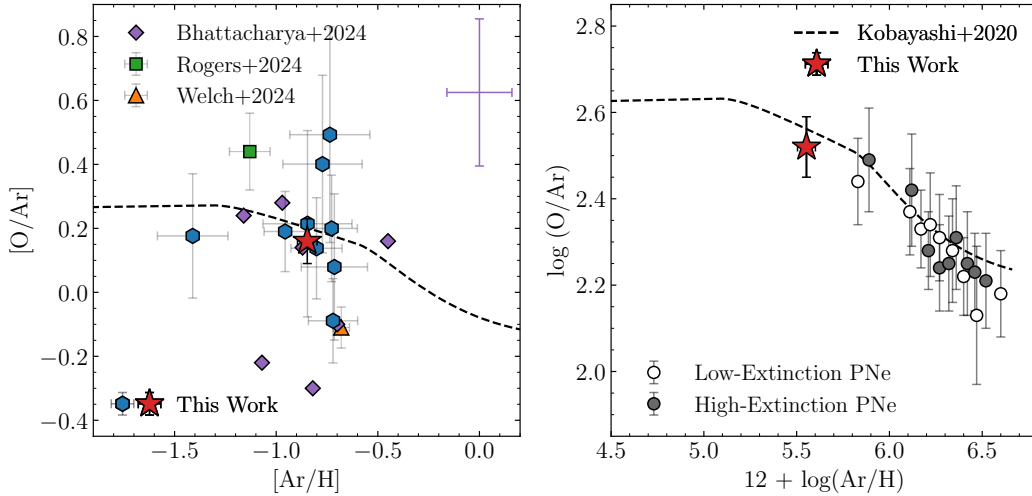


**Figure 5.** In the left panel we compare the O/Ar and Ar/H abundance ratios of our sample (blue hexagons) and the measurements of [Bhattacharya et al. \(2024\)](#) (purple diamonds), [Rogers et al. \(2024\)](#) (green square), and [Welch et al. \(2024\)](#) (orange triangle) to the [Kobayashi et al. \(2020b\)](#) chemical evolution model representative of the Milky Way. We show the median error of the [Bhattacharya et al. \(2024\)](#) points in the top right. To ensure an accurate comparison we have adopted the solar yields used by [Kobayashi et al. \(2020b\)](#), namely  $\log(O/H)_\odot = 8.76$  and  $\log(Ar/H)_\odot = 6.40$ . The majority of the EXCELS galaxies are consistent with supersolar O/Ar ratios, including the weighted average of the sample (red star), indicating a deficit in Ar in these systems. The EXCELS galaxies generally agree with the trend shown by the [Kobayashi et al. \(2020b\)](#) relationship, with outliers attributed to more complex enrichment scenarios or poor performance of the ICF at high metallicity. The sample-weighted average is consistent with the trend set by the M31 PNe data and the [Kobayashi et al. \(2020b\)](#) relationship, suggesting that high-redshift systems are on average evolving along similar pathways as local systems.

the [Kobayashi et al. \(2020b\)](#) model, generally falling close to the knee of the relation. Interestingly, this situation is consistent with the locations of  $z \simeq 3.5$  star-forming galaxies in the  $[Fe/H] - [O/Fe]$  plane, which are also observed to lie close to, or just beyond, the knee corresponding to the onset of SNe Ia enrichment (e.g. [Cullen et al. 2021](#); [Stanton et al. 2024](#)). This aligns with the expectation that young star-forming galaxies are yet to undergo significant SNe Ia enrichment. However, it is important to note that the [Kobayashi et al. \(2020b\)](#) model is not universal but is built specifically to match the abundance patterns observed in Milky Way stars. Galaxies falling above/below the [Kobayashi et al. \(2020b\)](#) model (e.g., EXCELS-121806 or the measurement of [Welch et al. 2024](#)) could be explained by assuming a different star-formation history. As an example, an infall of pristine gas between starbursts could serve to maintain the [O/Ar] abundance ratio but decrease the [Ar/H] ratio, leading to galaxies residing below the Milky Way relation ([Bhattacharya et al. 2024](#)). Nevertheless, this comparison demonstrates consistency between our data and the *expectations* for low-metallicity galaxies at early epochs under a sensible star-formation history assumption.

Furthermore, we find that our measurements are consistent with observations in the local Universe. In the right panel of Fig. 5, we compare the weighted-average abundances of our sample to measurements of planetary nebulae (PNe) in M31 from [Arnaboldi et al. \(2022\)](#). The PNe closely follow the decreasing branch of the [Kobayashi et al. \(2020b\)](#) model, indicative of an increase in SNe Ia enrichment causing a decrease in O/Ar at higher metallicity (i.e., increasing Ar/H). Our sample average lies at the natural extension of this sequence, falling closer to the knee of the relationship, reflecting an epoch of relatively little SNe Ia enrichment. These comparisons may suggest that, on average, high-redshift systems follow the same evolutionary pathways as in local ones, although direct comparisons such as these are not straightforward (Monty et al. in prep). At the very least, however, the consistent picture emerging between local obser-

vations, high-redshift observations, and the predictions of chemical evolution models, as suggested by Fig. 5, is reassuring.

#### 4.2 Neon

Ne is an example of a typical  $\alpha$ -element which is expected to be produced primarily by CCSNe with no production channel through SNe Ia ([Kobayashi et al. 2020b](#)). Although there is some evidence for excess Ne enrichment at high metallicities ( $12 + \log(O/H) \gtrsim 8.5$ ; [Kobayashi et al. 2020b](#); [Miranda-Pérez & Hidalgo-Gómez 2023](#); [Arellano-Córdova et al. 2024](#)), this should not be relevant for our low-metallicity  $z \simeq 4$  sample. As such, Ne acts as a useful control element; in contrast to Ar/O, the Ne/O ratio is *not* expected to evolve across cosmic time (e.g., [Arellano-Córdova et al. 2022](#)).

In Fig. 6 and Fig. 7 we show Ne/O as a function of redshift and  $12 + \log(O/H)$  (i.e., mirroring Figs. 3 and 4 for Ar). From Fig. 6 it can be seen that our sample and the majority of other high-redshift estimates are consistent with the solar value (e.g., [Arellano-Córdova et al. 2022](#); [Marques-Chaves et al. 2024](#); [Welch et al. 2024](#)). The weighted average of our new EXCELS sample is  $\langle \log(Ne/O) \rangle = -0.60 \pm 0.05$ , which is fully consistent with the solar value within  $< 1\sigma$ .

These results are also fully consistent with the results of [Arellano-Córdova et al. \(2024\)](#), who find an unweighted average of  $\langle \log(Ne/O) \rangle = -0.63 \pm 0.06$  for local galaxies in the CLASSY survey. It is worth noting that Ne/O measurements from local star-forming galaxies typically fall systematically below the solar value. For example, [Izotov et al. \(2006\)](#) find  $\langle \log(Ne/O) \rangle \simeq -0.75$  for a sample of metal-poor galaxies from SDSS. However, [Arellano-Córdova et al. \(2024\)](#) re-analysed these Ne/O ratios with updated atomic data (see also [Berg et al. 2015](#)), finding results consistent with the solar value ( $\langle \log(Ne/O) \rangle \simeq -0.65$ ).

However, [Isobe et al. \(2023b\)](#) report generally subsolar Ne/O

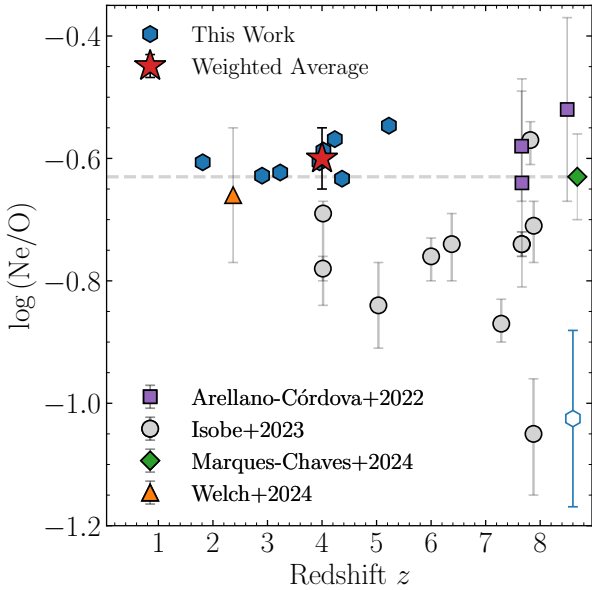


**Figure 6.** The  $\log(\text{Ne}/\text{O})$  abundance as a function of redshift for our sample (blue hexagons). We show the median average error bar in with an unfilled blue hexagon in the bottom right. For comparison, we show the direct-method measurements of Arellano-Córdova et al. (2022) (purple squares), Isobe et al. (2023b) (grey circles), Marques-Chaves et al. (2024) (green diamond) and Welch et al. (2024) (orange triangle). The weighted average of our measurements,  $\log(\text{Ne}/\text{O}) = -0.60 \pm 0.05$ , is shown with a red star at the median redshift of the sample. We denote the solar ratio,  $\log(\text{Ne}/\text{O})_{\odot} = -0.63$ , with a grey dashed line. Our Ne/O ratios show excellent consistency with the solar relation and local samples, suggesting O and Ne are enriched via similar pathways.

abundances for their galaxies at  $4 < z < 8$ . Their lowest estimates of  $\log(\text{Ne}/\text{O}) < -1.0$  can be attributed to the presence of massive ( $> 30M_{\odot}$ ) stellar populations (see Watanabe et al. 2024). However, it is unclear what drives their other Ne/O abundances to lower values than measured from other galaxy samples at similar redshifts. In either case, the Ne/O values at high-redshift are fully consistent with local estimates. Fig. 7 further highlights this point, where it can be seen that the Ne/O values we derive align with local star-forming galaxies from Arellano-Córdova et al. (2024) at all metallicities, in contrast to the offset in Ar/O shown in Fig. 4.

Our observations therefore support a scenario in which Ne acts as a pure  $\alpha$  element enriched mainly by CCSNe, whereas Ar has an additional - and significant - production channel via SNe Ia. As a result, local and high-redshift star-forming galaxies display similar Ne/O ratios, whereas the Ar/O ratio is lower in high-redshift systems as a result of the delayed onset of SNe Ia. This basic result is illustrated in Fig. 8, where we show the distributions of  $[\text{Ne}/\text{O}]$  and  $[\text{Ar}/\text{O}]$  for our sample compared to the CLASSY sample at  $z \approx 0$  (Arellano-Córdova et al. 2024). These results are in line with expectations based on the expected star-formation histories of  $z \approx 4$  star-forming galaxies combined with CCSNe and SNe Ia yield models (e.g. Kobayashi et al. 2020b). However, it is clear that the current sample sizes are relatively small. Moreover, as discussed in Section 2, the sample presented here is biased to above average SFRs compared to the full  $z \approx 4$  star-forming population. Therefore, more complete samples with direct O, Ne, and Ar abundance estimates

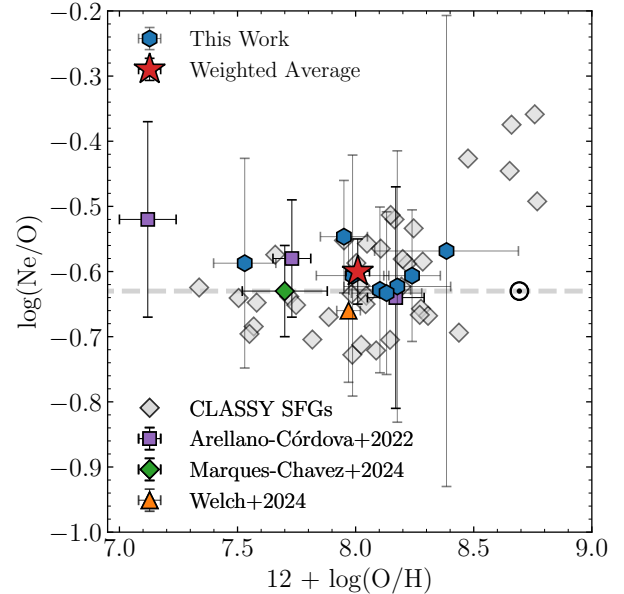


**Figure 7.** The Ne/O abundances of the EXCELS galaxies (blue hexagons) as a function of metallicity. For comparison, we plot the high-redshift measurements of Arellano-Córdova et al. (2022) (purple squares), Marques-Chaves et al. (2024) (green diamond) and Welch et al. (2024) (orange triangle). The local analogue CLASSY sample (Arellano-Córdova et al. 2024) is plotted in grey diamonds, and we denote the solar abundance with  $\odot$ , and the  $(\text{Ne}/\text{O})_{\odot}$  ratio with a grey dashed line. The weighted average of our sample (red star) is  $\langle \log(\text{Ne}/\text{O}) \rangle = -0.60 \pm 0.05$  and is consistent with the solar value within  $1\sigma$ . Across the entire  $\log(\text{O}/\text{H})$  range, the Ne/O ratio appears broadly constant and highly consistent with the solar value and local samples.

are required to confirm that these trends are characteristic of the full galaxy population at  $2 < z < 6$ .

## 5 DISCUSSION

In the following section, we discuss some important systematic uncertainties that may affect our measured abundance ratios, namely the assumed temperature structure, dust depletion, and the choice of ICF and atomic data. We limit our discussion here to the systematics as they relate to Ar abundances (although the same considerations also apply to Ne and, to a lesser extent, O).

### 5.1 Atomic data and ICFs

Our chosen set of atomic data (see Table 2) follows similar studies of high-redshift star-forming galaxies (e.g., Rogers et al. 2024). However, alternative data on transition probabilities and collision strengths exist. In particular, our main  $z \approx 0$  reference sample (CLASSY; Arellano-Córdova et al. 2024) use the collision strengths of Galavis et al. (1995) and the transition probabilities of Mendoza (1983) and Kaufman & Sugar (1986) for  $\text{Ar}^{2+}$  in their analysis. Switching to these atomic data, the average difference ( $\pm$  standard deviation) of the  $\log(\text{Ar}/\text{H})$  abundances we derive is  $0.04 \pm 0.09$  dex. This change is insufficient to align the average Ar abundance of our sample with the  $z \approx 0$  data and solar value.

We also explore different choices for the Ar ICF, considering

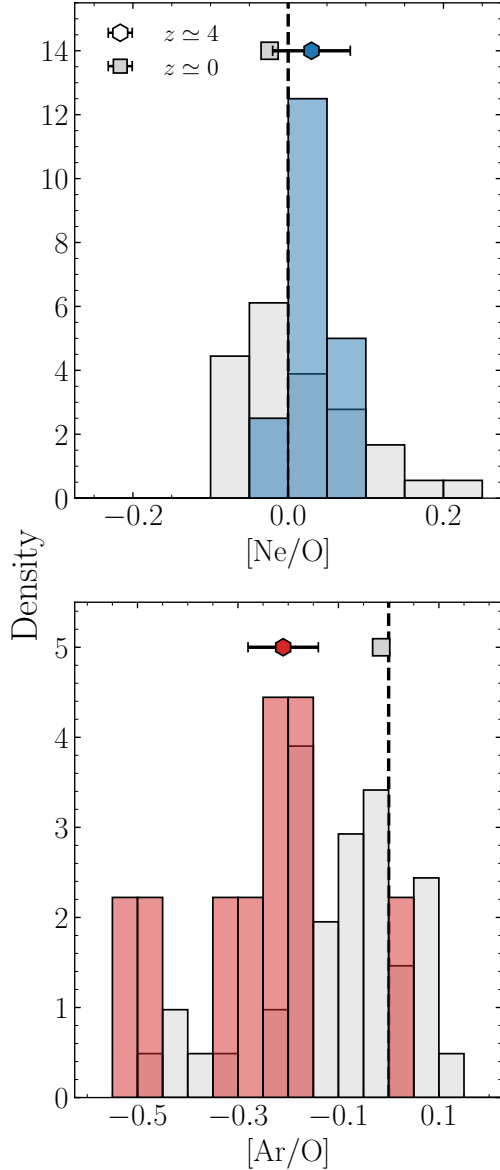


**Figure 8.** In the top panel we compare the  $[\text{Ne}/\text{O}]$  measurements of our sample (blue) to the  $z \simeq 0$  sample of CLASSY (grey; Arellano-Córdova et al. 2024). The weighted averages of each shown by a blue hexagon and grey square respectively. In the bottom panel we show the same but for  $[\text{Ar}/\text{O}]$ , with our sample coloured red in this case. The  $[\text{Ne}/\text{O}]$  ratio clearly shows no clear evolution at  $z \simeq 4$  compared to local star-forming galaxies, with fully consistent averages. In contrast,  $[\text{Ar}/\text{O}]$  shows an offset to lower values at higher redshifts. These trends are consistent with a scenario wherein Ne is enriched through the same channels as O, whilst Ar has a delayed secondary enrichment through SNe Ia.

the ICFs of Pérez-Montero et al. (2007) and Amayo et al. (2021). Applying either of these ICFs results in a slight increase in our measured Ar abundances; the Pérez-Montero et al. (2007) ICF increases  $\log(\text{Ar}/\text{H})$  by  $0.04 \pm 0.09$  dex whilst the Amayo et al. (2021) ICF results in an increase of  $0.04 \pm 0.13$  dex. Both of these offsets are again minor, and the resulting abundances are fully consistent with the abundances using the Izotov et al. (2006) ICF, and thus the deviation of Ar/O from the solar value cannot be attributed to the choice

of ICF. Taking combinations of the alternative ICFs and atomic data yields  $\langle \log(\text{Ar}/\text{O}) \rangle < -2.40$  which is still  $\simeq 2\sigma$  discrepant from the solar value.

## 5.2 Dust Depletion

Dust in the ISM can deplete heavy elements from the surrounding gas, with the degree of depletion depending on the condensation temperatures of each element (Savage & Sembach 1996; Groves et al. 2004). Both Ar and Ne are noble gases with low condensation temperatures (i.e., 47 K and 9 K) and, as such, should not condense and become trapped in dust grains within H II regions (Lodders 2003; Sofia 2004). However, O has a higher condensation temperature (180 K) and has been observed to deplete onto dust. For example, Peimbert & Peimbert (2010) measured O abundances in galactic and extragalactic H II regions, finding that O-depletion onto dust grains in systems with  $7.3 < 12 + \log(\text{O}/\text{H}) < 7.8$  decreases the measured  $\log(\text{O}/\text{H})$  by an average of  $0.09 \pm 0.03$  dex ( $\simeq 25$  per cent). Higher metallicity systems in the range  $8.3 < 12 + \log(\text{O}/\text{H}) < 8.8$  have a slightly larger fraction of their oxygen trapped in dust ( $0.11 \pm 0.03$  dex). Further analysis by Peña-Guerrero et al. (2012) finds that estimation of the true oxygen abundance of a system requires increasing the oxygen abundance by  $\simeq 0.10$  dex. Similarly, Gutkin et al. (2016) found that in order to accurately reproduce the expected optical emission line diagrams of star-forming galaxies in their models required a  $\simeq 30$  per cent depletion of O onto dust grains.

Throughout this work, we have followed the methodology of our main comparison samples and have chosen not to correct for the effect of O depletion. However, applying a dust correction would decrease the Ar/O ratio by 0.10 dex. This correction would only serve to increase the separation between the solar Ar/O ratio and local galaxies and thus strengthen our conclusions. A similar correction to the Ne/O ratio would bring our average below the solar ratio, but still consistent within  $< 2.3\sigma$ . Therefore, our results would not change - and if anything would be strengthened - by including dust depletion.

## 5.3 Temperature structure

The direct method approach for measuring chemical abundances relies on accurate temperature and density estimates. As discussed in Section 3.2, our abundance measurements are relatively insensitive to the exact density value within the low-density regime of our sample (i.e., as long as the density does not exceed  $\log(n_e/\text{cm}^{-3}) \simeq 3.5$ ). However, systematic differences in the electron temperatures assigned to each ionization zone can have a significant effect on the measured abundances. The fundamental, and mostly unavoidable, problem for high-redshift observations is that we often only have access to the high-ionization zone temperature via the auroral  $[\text{O III}]\lambda 4363$  line. In this situation, it is common practice, as we have done, to apply temperature scaling relationships to infer the temperatures of the other ionization zones. These relationships are derived either from photoionization models (e.g., Campbell et al. 1986; Garnett 1992) or low-redshift observations H II regions (e.g., Croxall et al. 2016; Arellano-Córdova & Rodríguez 2020; Rogers et al. 2021). However, whether these temperature scaling relations accurately describe H II regions in high-redshift galaxies has still not been robustly verified.

The recent analyses of Welch et al. (2024) and Rogers et al. (2024) serve to illustrate this issue. In both cases, access to deeper data allows these authors to measure the intermediate ionization zone temperature using the  $[\text{S III}]\lambda 6312$  auroral line. Rogers et al. (2024)

find a value consistent with local empirical relations and photoionization models, in which  $T_e[\text{SIII}] \simeq T_e[\text{OIII}]$ . In contrast, [Welch et al. \(2024\)](#) find  $T_e[\text{SIII}] \ll T_e[\text{OIII}]$  for the Sunburst Arc. Indeed, this is the main reason why [Welch et al. \(2024\)](#) derived a solar-like Ar/O ratio. Applying  $T_e[\text{SIII}] \simeq T_e[\text{OIII}]$  to the [Welch et al. \(2024\)](#) data yields  $\log(\text{Ar}/\text{O}) \simeq -2.4$ , more consistent with our analysis.

It is clear that the assumed temperature structure can cause significant variation in the measured abundances. Future JWST spectroscopic observations, with sufficient depth to robustly measure the temperatures of multiple ionization zones, are needed to test the validity of the commonly used  $T_e - T_e$  relations at high redshift. A caveat to the results presented here is that we *assume* current  $T_e - T_e$  relations are valid at  $z \simeq 4$ .

## 6 CONCLUSIONS

In this work we have presented direct O, Ar and Ne abundance measurements for nine star-forming galaxies in the redshift range  $1.8 < z < 5.3$  from the JWST EXCELS survey ([Carnall et al. 2024](#)). We have compared our sample with other high redshift and local samples from the literature to investigate the relationships between Ar/O, Ne/O and O/H. The primary motivation of the study has been to determine whether there is evidence for an Ar deficit in high-redshift galaxies as a result of significant Ar production via SNe Ia. Our main results are as follows:

(i) We find that the bulk of our sample exhibit Ar/O values below the solar value of  $\log(\text{Ar}/\text{O}_\odot) = -2.31$  (Figs. 3 and 4). The weighted average of our measurements is  $\langle \log(\text{Ar}/\text{O}) \rangle = -2.52 \pm 0.07$ , a  $\simeq 3\sigma$  offset below solar. On a linear scale, our result is  $\langle \text{Ar}/\text{O} \rangle = 0.62 \pm 0.10 (\text{Ar}/\text{O})_\odot$ , which is consistent with supernova yield models that predict  $\simeq 34$  per cent of Ar production occurs via SNe Ia, and implies that the ISM of star-forming galaxies at  $z \simeq 4$  are dominated by CCSNe products.

(ii) In contrast, we find no deviation from the solar value when considering the Ne/O ratio (Figs. 6 and 7). We find a weighted average Ne abundance of  $\langle \text{Ne}/\text{O} \rangle = 1.07 \pm 0.12 (\text{Ne}/\text{O})_\odot$ . This result implies that Ne can be considered a pure  $\alpha$ -element that follows the same enrichment pathways as O, as expected by models.

(iii) We have verified our results against a sample of local star-forming galaxies with similar total metallicity from the CLASSY survey ([Arellano-Córdova et al. 2024](#); Figs. 4, 7 and 8). Our sample shows similar Ne/O but lower Ar/O compared to these local star-forming analogues.

(iv) We have compared our measurements to the Milky Way chemical evolution model of [Kobayashi et al. \(2020b\)](#) as well as local measurements of PNe in M31 (Fig. 5). Our sample is generally in good agreement with the model predictions, which can be again interpreted as a lack of SNe Ia enrichment in high-redshift star-forming galaxies. We find that our average Ar/O estimate also lies at the extension of the sequence inferred from PNe in the [O/Ar]-[Ar/H] plane (Fig. 5). Taken together, these comparisons imply that the Ar deficit we observe is consistent with *both* local data and the predictions chemical evolution models.

(v) We have assessed the effect of systematic uncertainties related to ICFs, atomic data, and dust depletion on our main result. We find that, when combined, these affects can alter  $\log(\text{Ar}/\text{O})$  at the  $\simeq 0.1$  dex level, however there is no strong evidence to suggest that this would alter our main conclusions. Uncertainties in the temperature structure of high-redshift H II regions can potentially have a significant effect (as illustrated by the [Welch et al. 2024](#) result) and

verifying  $T_e - T_e$  relations should be a high priority of future JWST programmes.

This work constitutes a significant increase in the sample size of galaxies with robust Ar abundances beyond  $z > 2$ , and our initial results are consistent with a picture in which Ar is deficient in high-redshift star-forming galaxies due to delayed SNe Ia enrichment. These results corroborate independent analyses of the O/Fe ratio at similar redshifts ([Steidel et al. 2016](#); [Cullen et al. 2019](#); [Topping et al. 2020a](#); [Kashino et al. 2022](#); [Chartab et al. 2024](#); [Stanton et al. 2024](#)). However, the current number of galaxies with direct Ar abundances measurements remains small, and additional data, as well as continued work on ICFs, dust depletion and the temperature structure of high-redshift H II regions are still required to robustly confirm these trends. Nevertheless, our analysis demonstrates the potential for using JWST to unravel the detailed chemical enrichment patterns observed in the early Universe.

## ACKNOWLEDGEMENTS

T. M. Stanton, F. Cullen, K. Z. Arellano-Córdova and D. Scholte acknowledge support from a UKRI Frontier Research Guarantee Grant (PI Cullen; grant reference: EP/X021025/1). A. C. Carnall and S. Stevenson acknowledges support from a UKRI Frontier Research Guarantee Grant (PI Carnall, grant reference EP/Y037065/1). R. Beggley, C. Bondestam, C. T. Donnan, J. S. Dunlop, D. J. McLeod and R. J. McLure acknowledge the support of the Science and Technology Facilities Council. J. S. Dunlop also thanks the Royal Society for their support through a Royal Society Research Professorship. This research made use of the following software: MATPLOTLIB ([Hunter 2007](#)), PYNEB ([Luridiana et al. 2015](#)), NUMPY ([Harris et al. 2020](#)), DYNESTY ([Speagle 2020](#)) and MSAEXP ([Brammer 2023](#)). This research utilised NASA’s Astrophysics Data System Bibliographic Services. For the purpose of open access, the author has applied a Creative Commons Attribution (CC BY) licence to any Author Accepted Manuscript version arising from this submission.

## DATA AVAILABILITY

All data will be shared by the corresponding author upon reasonable request.

## REFERENCES

- Amayo A., Delgado-Inglada G., Stasińska G., 2021, *MNRAS*, **505**, 2361  
 Andrews B. H., Martini P., 2013, *ApJ*, **765**, 140  
 Arellano-Córdova K. Z., Rodríguez M., 2020, *MNRAS*, **497**, 672  
 Arellano-Córdova K. Z., et al., 2022, *ApJ*, **940**, L23  
 Arellano-Córdova K. Z., et al., 2024, *ApJ*, **968**, 98  
 Arnaboldi M., et al., 2022, *A&A*, **666**, A109  
 Asplund M., Amarsi A. M., Grevesse N., 2021, *A&A*, **653**, A141  
 Berg D. A., Skillman E. D., Croxall K. V., Pogge R. W., Moustakas J., Johnson-Groh M., 2015, *ApJ*, **806**, 16  
 Berg D. A., Chisholm J., Erb D. K., Skillman E. D., Pogge R. W., Olivier G. M., 2021, *ApJ*, **922**, 170  
 Berg D. A., et al., 2022, *ApJS*, **261**, 31  
 Bertin E., Arnouts S., 1996, *A&AS*, **117**, 393  
 Bhattacharya S., Arnaboldi M., Gerhard O., Kobayashi C., Saha K., 2024, *arXiv e-prints*, p. [arXiv:2408.13396](#)  
 Brammer G., 2023, *msaexp*: NIRSpec analysis tools, [doi:10.5281/zenodo.7299500](#)

- Branch M. A., Coleman T. F., Li Y., 1999, *SIAM Journal on Scientific Computing*, 21, 1
- Bruzual G., Charlot S., 2003, *MNRAS*, 344, 1000
- Campbell A., Terlevich R., Melnick J., 1986, *MNRAS*, 223, 811
- Cardelli J. A., Clayton G. C., Mathis J. S., 1989, *ApJ*, 345, 245
- Carnall A. C., McLure R. J., Dunlop J. S., Davé R., 2018, *MNRAS*, 480, 4379
- Carnall A. C., et al., 2024, *MNRAS*, 534, 325
- Chartab N., Newman A. B., Rudie G. C., Blanc G. A., Kelson D. D., 2024, *ApJ*, 960, 73
- Clarke L., et al., 2023, *ApJ*, 957, 81
- Clarke L., Shapley A. E., Sanders R. L., Topping M. W., Brammer G. B., Bento T., Reddy N. A., Kehoe E., 2024, *arXiv e-prints*, p. arXiv:2406.05178
- Croxall K. V., Pogge R. W., Berg D. A., Skillman E. D., Moustakas J., 2016, *ApJ*, 830, 4
- Cullen F., Cirasuolo M., McLure R. J., Dunlop J. S., Bowler R. A. A., 2014, *MNRAS*, 440, 2300
- Cullen F., et al., 2019, *MNRAS*, 487, 2038
- Cullen F., et al., 2021, *MNRAS*, 505, 903
- Curti M., et al., 2024, *A&A*, 684, A75
- Erb D. K., Shapley A. E., Pettini M., Steidel C. C., Reddy N. A., Adelberger K. L., 2006, *ApJ*, 644, 813
- Froese Fischer C., Tachiev G., 2004, *Atomic Data and Nuclear Data Tables*, 87, 1
- Galavis M. E., Mendoza C., Zeppen C. J., 1995, *A&AS*, 111, 347
- Garnett D. R., 1992, *AJ*, 103, 1330
- Groves B. A., Dopita M. A., Sutherland R. S., 2004, *ApJS*, 153, 9
- Gutkin J., Charlot S., Bruzual G., 2016, *MNRAS*, 462, 1757
- Hao C.-N., Kennicutt R. C., Johnson B. D., Calzetti D., Dale D. A., Moustakas J., 2011, *ApJ*, 741, 124
- Harris C. R., et al., 2020, *Nature*, 585, 357
- Horne K., 1986, *PASP*, 98, 609
- Hunter J. D., 2007, *Computing in Science & Engineering*, 9, 90
- Irimia A., Froese Fischer C., 2005, *Phys. Scr.*, 71, 172
- Isobe Y., Ouchi M., Nakajima K., Harikane Y., Ono Y., Xu Y., Zhang Y., Umeda H., 2023a, *ApJ*, 956, 139
- Isobe Y., et al., 2023b, *ApJ*, 959, 100
- Izotov Y. I., Stasińska G., Meynet G., Guseva N. G., Thuan T. X., 2006, *A&A*, 448, 955
- James B. L., et al., 2022, *ApJS*, 262, 37
- Jeong M.-S., et al., 2020, *ApJ*, 902, L16
- Kashino D., et al., 2022, *ApJ*, 925, 82
- Kaufman V., Sugar J., 1986, *Journal of Physical and Chemical Reference Data*, 15, 321
- Kisielius R., Storey P. J., Ferland G. J., Keenan F. P., 2009, *MNRAS*, 397, 903
- Kobayashi C., Leung S.-C., Nomoto K., 2020a, *ApJ*, 895, 138
- Kobayashi C., Karakas A. I., Lugaro M., 2020b, *ApJ*, 900, 179
- Kroupa P., 2001, *MNRAS*, 322, 231
- Lara-López M. A., et al., 2010, *A&A*, 521, L53
- Lodders K., 2003, *ApJ*, 591, 1220
- Luridiana V., Morisset C., Shaw R. A., 2015, *A&A*, 573, A42
- Maiolino R., Mannucci F., 2019, *A&ARv*, 27, 3
- Maiolino R., et al., 2008, *A&A*, 488, 463
- Mannucci F., Cresci G., Maiolino R., Marconi A., Gnerucci A., 2010, *MNRAS*, 408, 2115
- Marques-Chaves R., et al., 2024, *A&A*, 681, A30
- Maseda M. V., et al., 2023, *ApJ*, 956, 11
- McClymont W., et al., 2024, *arXiv e-prints*, p. arXiv:2405.15859
- McLaughlin B. M., Lee T.-G., Ludlow J. A., Landi E., Loch S. D., Pindzola M. S., Ballance C. P., 2011, *Journal of Physics B Atomic Molecular Physics*, 44, 175206
- Méndez-Delgado J. E., et al., 2023, *MNRAS*, 523, 2952
- Mendoza C., 1983, *Proceedings of the International Astronomical Union*, 103, 143
- Mendoza C., Zeppen C. J., 1983, *MNRAS*, 202, 981
- Mingozzi M., et al., 2022, *ApJ*, 939, 110
- Miranda-Pérez B. E., Hidalgo-Gómez A. M., 2023, *ApJ*, 952, 76
- Moustakas J., Buhler J., Scholte D., Dey B., Khederlarian A., 2023, *Fast-SpecFit: Fast spectral synthesis and emission-line fitting of DESI spectra*, Astrophysics Source Code Library, record ascl:2308.005
- Mucciarelli A., Minelli A., Bellazzini M., Lardo C., Romano D., Origlia L., Ferraro F. R., 2023, *A&A*, 671, A124
- Munoz Burgos J. M., Loch S. D., Ballance C. P., Boivin R. F., 2009, *A&A*, 500, 1253
- Nakane M., et al., 2024, *arXiv e-prints*, p. arXiv:2407.14470
- Peña-Guerrero M. A., Peimbert A., Peimbert M., 2012, *ApJ*, 756, L14
- Peimbert A., Peimbert M., 2010, *ApJ*, 724, 791
- Pérez-Montero E., Hägele G. F., Contini T., Díaz Á. I., 2007, *MNRAS*, 381, 125
- Péroux C., Howk J. C., 2020, *ARA&A*, 58, 363
- Reddy N. A., et al., 2020, *ApJ*, 902, 123
- Rogers N. S. J., Skillman E. D., Pogge R. W., Berg D. A., Moustakas J., Croxall K. V., Sun J., 2021, *ApJ*, 915, 21
- Rogers N. S. J., Skillman E. D., Pogge R. W., Berg D. A., Croxall K. V., Bartlett J., Arellano-Córdova K. Z., Moustakas J., 2022, *ApJ*, 939, 44
- Rogers N. S. J., Strom A. L., Rudie G. C., Trainor R. F., Raptis M., von Raesfeld C., 2024, *ApJ*, 964, L12
- Salim S., Boquien M., Lee J. C., 2018, *ApJ*, 859, 11
- Sanders R. L., et al., 2021, *ApJ*, 914, 19
- Sanders R. L., et al., 2024, *arXiv e-prints*, p. arXiv:2408.05273
- Savage B. D., Sembach K. R., 1996, *ARA&A*, 34, 279
- Scarlata C., Hayes M., Panagia N., Mehta V., Haardt F., Bagley M., 2024, *arXiv e-prints*, p. arXiv:2404.09015
- Scholte D., et al., 2024, *arXiv e-prints*, p. arXiv:2408.03996
- Shapley A. E., et al., 2019, *ApJ*, 881, L35
- Shapley A. E., et al., 2024, *arXiv e-prints*, p. arXiv:2407.00157
- Sofia U. J., 2004, in Witt A. N., Clayton G. C., Draine B. T., eds, *Astronomical Society of the Pacific Conference Series Vol. 309, Astrophysics of Dust*. p. 393
- Speagle J. S., 2020, *MNRAS*, 493, 3132
- Speagle J. S., Steinhardt C. L., Capak P. L., Silverman J. D., 2014, *ApJS*, 214, 15
- Stanton T. M., et al., 2024, *MNRAS*, 532, 3102
- Steidel C. C., Strom A. L., Pettini M., Rudie G. C., Reddy N. A., Trainor R. F., 2016, *ApJ*, 826, 159
- Storey P. J., Hummer D. G., 1995, *MNRAS*, 272, 41
- Storey P. J., Sochi T., Badnell N. R., 2014, *MNRAS*, 441, 3028
- Strom A. L., Rudie G. C., Steidel C. C., Trainor R. F., 2022, *ApJ*, 925, 116
- Strom A. L., et al., 2023, *ApJ*, 958, L11
- Tayal S. S., Zatsariny O., 2010, *ApJS*, 188, 32
- Topping M. W., Shapley A. E., Reddy N. A., Sanders R. L., Coil A. L., Kriek M., Mobasher B., Siana B., 2020a, *MNRAS*, 495, 4430
- Topping M. W., Shapley A. E., Reddy N. A., Sanders R. L., Coil A. L., Kriek M., Mobasher B., Siana B., 2020b, *MNRAS*, 499, 1652
- Topping M. W., et al., 2024, *arXiv e-prints*, p. arXiv:2407.19009
- Tremonti C. A., et al., 2004, *ApJ*, 613, 898
- Virtanen P., et al., 2020, *Nature Methods*, 17, 261
- Watanabe K., et al., 2024, *ApJ*, 962, 50
- Weinberg D. H., Andrews B. H., Freudenburg J., 2017, *ApJ*, 837, 183
- Welch B., et al., 2024, *arXiv e-prints*, p. arXiv:2405.06631
- Zinchenko I. A., Sobolenko M., Vílchez J. M., Kehrig C., 2024, *A&A*, 690, A28

## APPENDIX A: ZOOM-INS ON [O III] $\lambda$ 4363 AND [Ar III] $\lambda$ 7135

In Figure A1, we show zoom ins on the individual emission line fits for the key emission lines for this study. Each window is continuum normalised with the best fitting profile overplotted. Above each line, we show a cut out of the 2D spectrum.

This paper has been typeset from a  $\text{\LaTeX}$  file prepared by the author.

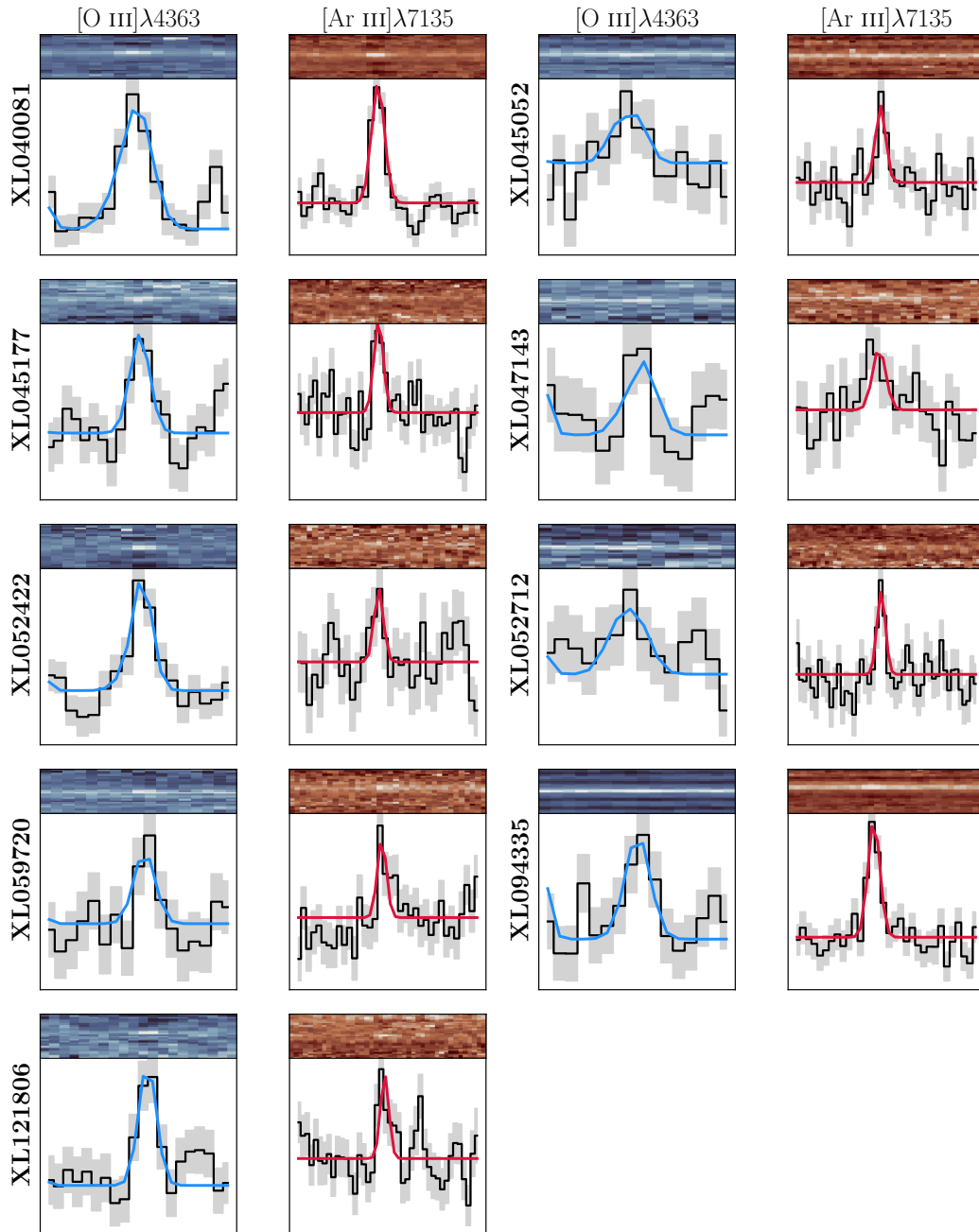


**Figure A1.** Zoom-ins on the principal faint emission lines of our sample. The continuum-normalised underlying spectrum is plotted in black, with the uncertainty on the spectrum is shaded in grey. [O III]λ4363 fits are shown in blue and [Ar III]λ7135 fits in red. Above each window, we show the corresponding 2D spectra.